processes

MDPI

Article

Research on the Impact Resistance of Sandwich-Structured Battery Pack Protective Plates

Jun Zhou [1], Changjie Luo [1,*], Ruilin Shen [1], Fengqiang Zhang [1], Wenze Yu [1], Mingming Zhang [2] and Weiliang Liao [2]

[1] Shenzhen CANSINGA Technology Co., Ltd., Shenzhen 518000, China; j.zhou@cansinga.com (J.Z.); srlrr490823@163.com (R.S.); zhangfengqiang163@163.com (F.Z.); wz.yu@cansinga.com (W.Y.)
[2] College of Artificial Intelligence, Harbin Institute of Technology, Shenzhen 518055, China; mmzhang@hit.edu.cn (M.Z.); wl.liao@stu.hit.edu.cn (W.L.)
* Correspondence: cj.luo@cansinga.com

Abstract: With the continuous development of the new energy vehicle industry, in order to further improve the safety and range of electric vehicles, vehicle lightweighting has been a key focus of major car companies. However, research on lightweighting and the impact protection effect of battery pack protective plates is lacking. The bottom protective plate of the battery pack in this study has a sandwich-type multi-layer structure, which is mainly composed of upper and lower glass-fiber-reinforced resin protective layers, steel plate impact resistant layers, and honeycomb buffer layers. In order to study the relationship between the impact damage response and material characteristics of the multi-material battery pack protective plate, a matrix experimental design was adopted in this study to obtain the energy absorption ratio of different material properties when the protective plate is subjected to impact damage. This work innovatively used a low-cost equivalent model method. During the drop hammer impact test, a 6061-T6 aluminum plate in direct contact with the lower part of the bottom guard plate test piece was used to simulate the deformation of the water-cooled plate in practical applications. High-strength aluminum honeycomb was arranged below the aluminum plate to simulate the deformation of the battery cell. This method provides a scientific quantitative standard for evaluating the impact resistance performance of the protective plate. The most preferred specimen in this work had a surface depression deformation of only 8.44 mm after being subjected to a 400 J high-energy impact, while the simulated water-cooled plate had a depression deformation of 4.07 mm. Among them, the high-strength steel plate played the main role in absorbing energy during the impact process, absorbing energy. It can account for about 34.3%, providing reference for further characterizing the impact resistance performance of the protective plate under different working conditions. At the same time, an equivalence analysis of the damage mode between the quasi-static indentation test and the dynamic drop hammer impact test was also conducted. Under the same conditions, the protective effect of the protective plate on impact damage was better than that of static pressure marks. From the perspective of energy absorption, the ratio coefficient of the two was about 1.2~1.3.

Keywords: aluminum honeycomb; sandwich composite panel; impact resistance; quasi-static indentation; impact energy

check for updates

Academic Editors: Wai Sze Yip, Zejia Zhao and Guoqing Zhang

Received: 3 April 2025
Revised: 1 May 2025
Accepted: 8 May 2025
Published: 23 May 2025

Citation: Zhou, J.; Luo, C.; Shen, R.; Zhang, F.; Yu, W.; Zhang, M.; Liao, W. Research on the Impact Resistance of Sandwich-Structured Battery Pack Protective Plates. *Processes* **2025**, *13*, 1639. https://doi.org/10.3390/pr13061639

Copyright: © 2025 by the authors. Licensee MDPI, Basel, Switzerland. This article is an open access article distributed under the terms and conditions of the Creative Commons Attribution (CC BY) license (https://creativecommons.org/licenses/by/4.0/).

1. Introduction

The automotive industry is undergoing a significant transformation driven by the rapid advancement and increasing adoption of new energy technologies, particularly electric vehicles (EVs) [1,2]. This surge in the global market share of EVs underscores the critical importance of ensuring the safety and reliability of their core power source: the battery pack [3,4]. In contemporary EV design, battery packs are typically positioned in the vehicle underbody to optimize weight distribution and enhance overall vehicle safety [5,6]. However, this placement also renders them a potentially vulnerable point, susceptible to mechanical damage from various external factors [7,8].

The mechanical integrity and robust protection of these battery packs are of paramount importance due to the potential for cascading failures if compromised [9,10]. Damage to battery cells can lead to severe safety hazards [11], including thermal runaway, fire, or explosion [12], posing significant risks to vehicle occupants and the surrounding environment [13]. Consequently, the design and implementation of effective battery protection systems are crucial for the widespread acceptance and safe operation of electric vehicles [14]. Regulatory bodies and industry standards are increasingly emphasizing the safety aspects of EV batteries, further highlighting the necessity for advanced protection solutions.

Traditional approaches to battery protection often involve the use of single-layer plates constructed from aluminum alloys or other metallic materials [15]. While these materials offer a basic level of shielding, they possess inherent limitations that can compromise their effectiveness in real-world scenarios [16]. These limitations include susceptibility to corrosion, insufficient surface strength to withstand abrasive forces, and poor wear resistance over extended periods [17]. As shown in Figure 1, there are currently four commonly used designs for electric vehicle bottom guards. The first-generation guard (Option 1) only contained a 2 mm steel/aluminum alloy protective layer, with poor impact strength of only about 120 J, and is currently on the brink of elimination. The more popular solution nowadays is the honeycomb sandwich composite panel, which includes a simple sandwich structure of fiberglass PP resin skin and PP plastic honeycomb. Although the density of the protective panel surface of this solution can be significantly reduced to one-quarter compared to the aluminum alloy protective layer, the impact resistance has not been improved. Recently, the structural schemes of the two protective plates have been further improved to enhance their impact resistance performance, with a maximum tolerance of 300 J peak impact energy. However, under the same conditions, the thickness of the protective plate has reached nearly 10 mm, which is also a significant challenge for the increasingly tight space of the tram chassis. Option 3 enhances the overall energy absorption effect of the protective plate by adding high-strength steel plates as the main role of energy absorption in the simple sandwich structure of Option 2. In Option 4, MPP foam cushioning material is used instead of honeycomb material, which can ensure the same impact strength while slightly reducing the surface density of the protective plate.

Furthermore, battery pack protection plates are frequently subjected to complex dynamic loads arising from road irregularities, vibrations experienced during transit, and unexpected impacts from road debris or collisions [18]. These intricate loading conditions can induce localized stress concentrations and lead to global structural deformation of the protection plate, thereby diminishing its capacity to adequately safeguard the sensitive battery system [19].

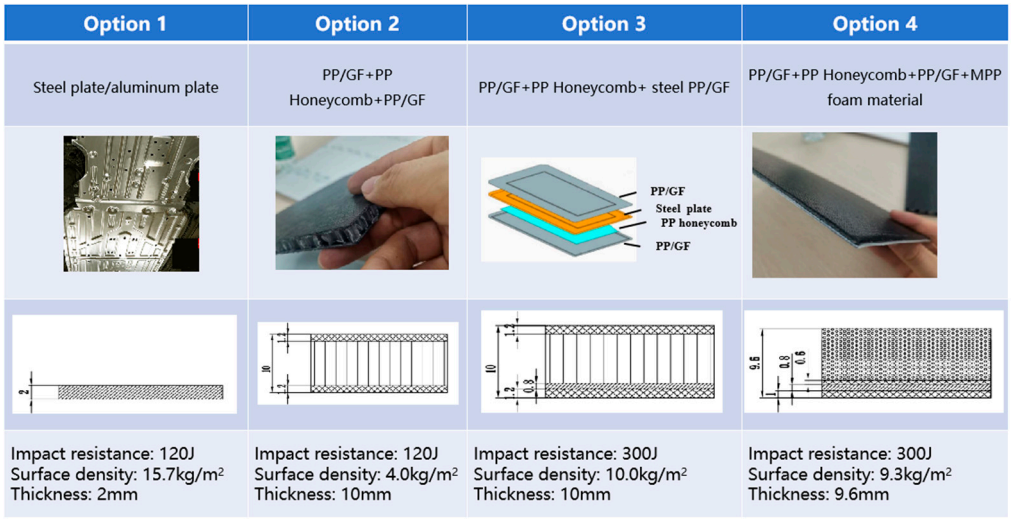

Figure 1. Comparison of structural design schemes for automotive bottom guards from different manufacturers.

Driven by the concurrent demands of extending the driving range of EVs and reducing the overall vehicle weight, manufacturers are increasingly adopting thinner and lighter protective designs [20]. This trend, while beneficial for vehicle efficiency and performance, presents a significant engineering challenge. As the protective plates become thinner to meet weight reduction targets, their inherent resistance to impact-induced deformation and potential penetration by foreign objects correspondingly decreases [21]. This necessitates the exploration and implementation of advanced materials and structural designs that can offer enhanced protection without adding excessive weight to the vehicle.

To address the limitations of traditional protection methods and the challenges posed by lightweighting trends [22], recent research efforts have focused on the development and application of multi-material composite structures, with a particular emphasis on sandwich-structured designs. These advanced configurations strategically combine high-performance materials, such as glass-fiber-reinforced resin skins [23], high-strength steel plates, and lightweight aluminum honeycomb cores [24], to effectively absorb and dissipate impact energy while maintaining the overall structural integrity of the battery pack [25]. Such structures offer the dual advantages of reduced weight compared to traditional metallic solutions and enhanced energy absorption capabilities, which are crucial for both passive safety in the event of a collision and the overall performance characteristics of the electric vehicle [26].

Furthermore, the application of advanced simulation techniques and comprehensive experimental investigations has provided valuable insights into the complex failure mechanisms exhibited by sandwich composites when subjected to dynamic loading conditions [27,28]. Studies conducted over the past five years have consistently highlighted the critical role of core layer thickness, the specific stacking sequence of the constituent materials, and the quality of the adhesive bonding between layers in determining the overall impact resistance of these sophisticated systems [29]. The intricate interplay of these factors not only governs the initiation of localized damage at the point of impact but also significantly influences the subsequent propagation of cracks and delamination across the various composite layers [30]. Therefore, a thorough and detailed understanding of the underlying energy absorption mechanisms and the resulting failure modes at the micro- and macrolevels is absolutely critical for the effective development of next-generation battery pack protection systems that can meet the ever-increasing demands of the electric vehicle industry [31].

At present, there is relatively little research on the mechanism of impact deformation of sandwich-type composite panels with multi-layer structures (four or more layers, including metal honeycomb), and the mainstream bottom protective panels in the market generally have an impact strength of no more than 300 J. There is also a lack of scientific and quantitative evaluation methods for the impact strength of protective panels in the industry. This study used a low-cost equivalent simulation substitution method, simulated the soft support of battery packs with high-strength aluminum honeycomb, and simulated water-cooled panels with 6061 series aluminum alloy to conduct matrix drop-hammer impact tests on each layer of materials, pairwise composites, and final product protective panels. Combined with static compression analysis methods, the damage mode and failure mechanism of sandwich-type composite panels were studied, providing a basis for the development of battery pack protective panels with high impact resistance and lightweight design in the future. The results obtained from this integrated experimental approach are anticipated to offer a comprehensive framework for optimizing key design parameters, thereby contributing to the enhancement of safety standards and overall performance in modern electric vehicles.

2. Drop-Weight Impact Test

The drop-weight impact test is used to assess the energy absorption capability of battery protective plates for new energy vehicles by measuring the variation in energy during impact. Upon impact, the protective plate absorbs part of the energy, thereby reducing the amount transmitted to the battery pack. During testing, the protective plate may undergo deformation or even damage. By analyzing the extent of deformation and failure modes, the load-bearing capacity and toughness of the plate under impact loading can be evaluated. Plates exhibiting minimal deformation and lower damage severity generally demonstrate superior impact resistance.

In this study, drop-weight impact tests were conducted at varying energy levels, ranging from 50 J to 400 J. We chose the impact energy range of 50–400 J (with a resolution of 50 J), which is based on the impact energy that may occur under daily driving conditions. For example, if small stones on the road collide with the bottom guard, the impact energy may be within 50 J. In addition, 150 J is the drop-hammer impact energy standard specified in the national standard, while 300 J is the impact energy tolerance standard of our competitors in the industry. An impact of 400 J is the standard that can withstand the deformation of the water-cooled plate depression less than 4 mm under our preferred solution. The impact energy was controlled by adjusting the drop height (as shown in Table 1, with corrected heights, including the hammer length). The specimens were 300 mm × 300 mm in size, with a nominal thickness ranging from 6.8 mm to 7.2 mm.

Table 1. Relationship between impact energy and vertical height.

Impact Energy (J)	Height (m)	Correction Height (m)	Falling Speed (m/s)
400	2.72	3.07	7.75
300	2.04	2.39	6.84
200	1.36	1.71	5.78
100	0.68	1.03	4.48
50	0.34	0.69	3.66

The drop-weight impact tests were performed in accordance with the ASTM D7136 standard [32], using a custom-built impact testing apparatus (Figure 2). The specimens were secured with four-corner clamping, and the hammerhead was made of # 45 steel, featuring a hemispherical bottom with a diameter of 25 mm and a mass of 15 kg. At an impact energy of 400 J, the corresponding drop velocity was approximately 7.75 m/s.

On the basis of improving the ASTMD 7136 experimental standard, we also refer to the industry standard "Requirements and Test Methods for Bottom Anti Collision Capacity of Pure Electric Passenger Vehicles" released by the Chinese Society of Automotive Engineers in 2021. Therefore, the specific requirements for the drop-hammer impact test in this study are shown in Table 2.



(**a**) (**b**)

Figure 2. Drop-hammer impact testing apparatus: (**a**) drop-hammer device; (**b**) guard sample and fixture.

Table 2. Drop-hammer impact test method. (# 45 steel represents 0.45% carbon steel).

Number	Project	Parameters
1	Impact head form	The front end of the impact head is hemispherical, with a size of 25 mm and a mass of 15 kg, and the material used is # 45 steel.
2	Impact direction	Perpendicular to the bottom guard plate
3	Impact locations	Impact locations shall not be less than 300 mm, with a geometric center
4	Impact energy	400 ± 5 J

In the Drop-Weight Impact Test Standard, the protective plate sample is placed horizontally on the base of the apparatus. A 1.5 mm thick aluminum plate (6061-T6) was positioned directly beneath the protective plate to simulate the deformation of the external water-cooling plate of the battery pack. Below the aluminum plate, a 50 mm thick soft-support aluminum honeycomb with a static compressive strength of 12 MPa (±1 MPa) was placed to simulate the deformation of the battery core, as shown in Figure 3.

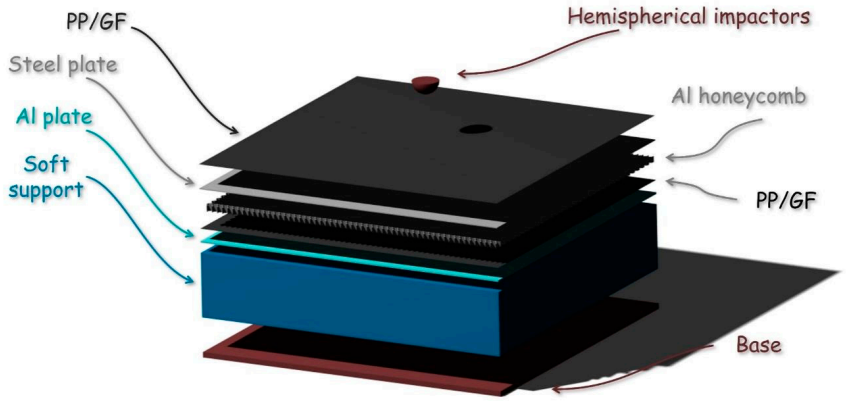

Figure 3. Schematic of the protection plate structure.

In research work, the impact energy is converted from the gravitational potential energy of the falling hammer. In order to ensure that the falling speed is as low as possible,

we added a movable pulley to the hammer energy storage mechanism to ensure that the hammer is in a free-fall state during the falling process. As shown in Table 3, we used a modified polyolefin hot-melt adhesive resin, with the model FP3218LC as the adhesive, to bond the layers of the protective plate, including between the PP/GF composite material and high-strength steel plate, between the high-strength plate and aluminum honeycomb, and between the aluminum honeycomb and PP/GF composite material. During the hot-pressing of a multi-material composite, the temperature needs to be controlled at 180–220 °C, and the composite pressure needs to be between 0.2 and 0.4MPa. The thickness of this adhesive film is only 0.2 mm, providing excellent bonding durability. In addition, the simulated water-cooled plate in direct contact with the protective plate specimen was not bonded with any adhesive, including the direct contact between the bottom simulated battery cell and the water-cooled plate. During the test, the protective plate, water-cooled plate, and battery cell components were fixed in a four-corner manner through a quick clamp of the base.

Table 3. Physical properties of adhesive on each layer of protective board.

Project	Unit	Typical Values
Visual inspection of appearance	/	Natural color adhesive film
Density	g/cm^3	0.892
Melt index (230 °C, 2.16 kg)	g/10 min	5.2
Melting point	°C	159
Vicat softening point	°C	106
Tensile strength MPa	MPa	20
Tensile elongation at break	%	600
Adhesive film thickness	mm	0.18~0.20

2.1. Single-Material Testing

To examine the contribution of each layer in a multi-material composite protective plate to the overall energy absorption, each layer of the plate was isolated and individually tested using drop-weight impact tests. The indentation deformation of each material was measured with a depth gauge, and the corresponding indentation on the aluminum plate was recorded. This allowed for the determination of the maximum critical failure values and energy absorption performance of each material layer under varying impact energy levels. We determined a sample size of five for each group based on statistical principles and preliminary test results to ensure the representativeness of the data. Each test was repeated at least twice, covering different testing environments and operators to eliminate random errors and system biases.

Polypropylene reinforced with glass fiber (PP/GF) was used for the upper and lower skins of the protective plate. During the drop-weight impact test, it was the first layer the hammer contacted and the first to undergo fracture and penetration [33]. As shown in the data in Figure 4, increasing the thickness of PP/GF enhanced its resistance to the impact of the hammer (here, "PP/GF-AP" refers to the aluminum plate in contact with the PP/GF layer). At an impact energy of 200 J, both thicknesses of PP/GF exhibited significant fracture failure. However, at impact energies of 100 J or below, the 1.0 mm thick PP/GF resulted in a slightly smaller indentation on the aluminum plate (approximately 2% less) compared to the 0.6 mm thick PP/GF. For a 300 mm × 300 mm specimen, the mass difference between the two PP/GF thicknesses was approximately 40 g. Therefore, using 1.0 mm thick PP/GF for the upper skin and 0.6 mm thick PP/GF for the lower skin (which deforms later) is an effective strategy for reducing weight while improving efficiency.

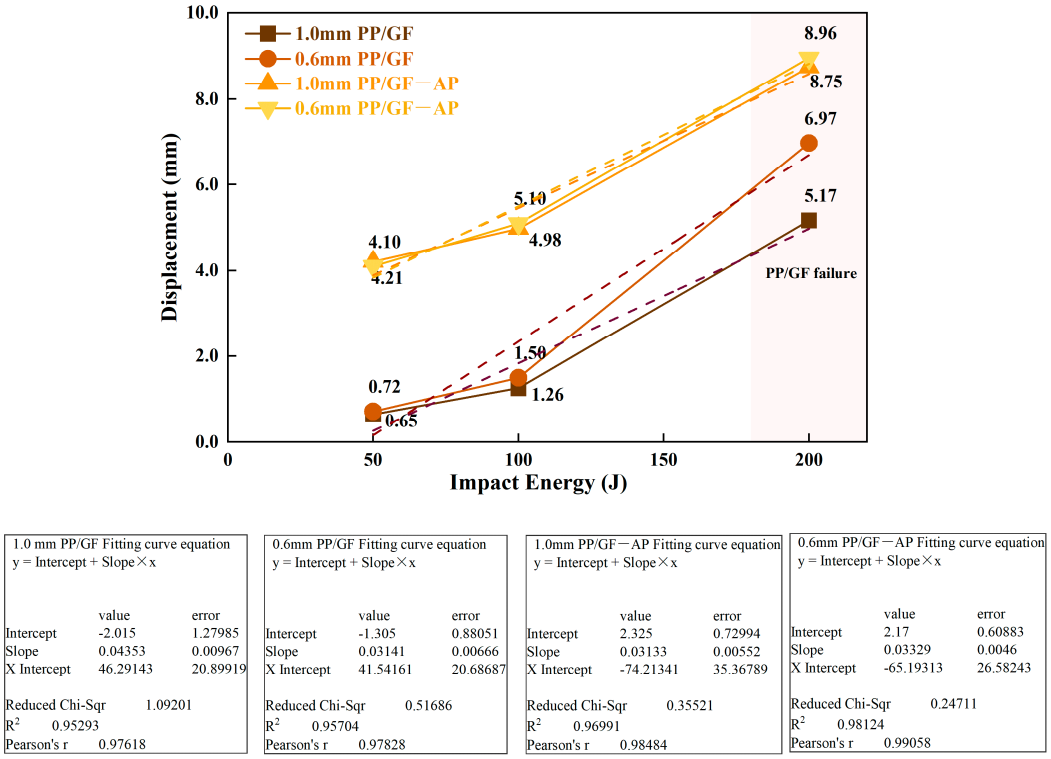

1.0 mm PP/GF Fitting curve equation
y = Intercept + Slope×x

	value	error
Intercept	-2.015	1.27985
Slope	0.04353	0.00967
X Intercept	46.29143	20.89919

Reduced Chi-Sqr	1.09201
R^2	0.95293
Pearson's r	0.97618

0.6mm PP/GF Fitting curve equation
y = Intercept + Slope×x

	value	error
Intercept	-1.305	0.88051
Slope	0.03141	0.00666
X Intercept	41.54161	20.68687

Reduced Chi-Sqr	0.51686
R^2	0.95704
Pearson's r	0.97828

1.0mm PP/GF—AP Fitting curve equation
y = Intercept + Slope×x

	value	error
Intercept	2.325	0.72994
Slope	0.03133	0.00552
X Intercept	-74.21341	35.36789

Reduced Chi-Sqr	0.35521
R^2	0.96991
Pearson's r	0.98484

0.6mm PP/GF—AP Fitting curve equation
y = Intercept + Slope×x

	value	error
Intercept	2.17	0.60883
Slope	0.03329	0.0046
X Intercept	-65.19313	26.58243

Reduced Chi-Sqr	0.24711
R^2	0.98124
Pearson's r	0.99058

Figure 4. Impact resistance of PP/GF with varying thicknesses. (The dashed lines represent the fitting curve between the impact energy of 200 J, 300 J, and 400 J and the deformation of the indentation).

Aluminum honeycomb materials exhibit remarkable properties, such as high wind pressure resistance, vibration damping, sound insulation, thermal insulation, flame retardancy, and high specific strength. These materials constitute the thickest component in a multi-material protective plate. Typically, the honeycomb core has a thickness of 5 mm and plays a crucial role in energy absorption and buffering. To assess the performance of aluminum honeycomb with varying static compressive strengths in the composite structure of the battery protective plate, impact tests were first conducted on honeycomb blocks with different static compressive strengths. The deformation of the aluminum plate in direct contact with the honeycomb served as a reference for evaluating the deformation of the battery water-cooling plate.

Based on the analysis presented in Figure 5a, the aluminum honeycomb core with a static compressive strength of 12 MPa (±1 MPa) is prone to penetration failure when subjected to impact energies exceeding 200 J. In contrast, Figure 5b demonstrates that the aluminum honeycomb with a static compressive strength of 18 MPa (±1 MPa) performed effectively under an impact energy of 100 J. Accordingly, the penetration behavior of honeycombs with varying static compressive strengths under impact was compiled. Assuming no penetration occurs, the compression ratio of the honeycomb core was estimated to be between 70% and 80%, based on the measured indentation of the honeycomb core and the contacting aluminum plate. During the quasi-static response, the honeycomb exhibited three main stages: the elastic stage, the plateau stress stage, and the densification stage. In the plateau stress stage, the deformation gradually increases as the structure yields, undergoes plastic collapse, and is ultimately crushed, thereby absorbing a significant amount of energy. At the end of the plateau, the honeycomb structure densifies, causing the slope of the curve to steepen and the stress to increase rapidly—an essential phase for energy absorption. Furthermore, flat compression tests were conducted on aluminum honeycomb and MPP panels of various thicknesses with a loading rate of 20 mm/min (without pre-weakening the honeycomb surface). From Figure 6, the static compressive

strength of the aluminum honeycomb core (ALHC curve) was found to be approximately 16 MPa. As is shown in Table 4, compared to compressible core materials of similar thickness, such as MPP, which have a compression ratio close to 90%, the aluminum honeycomb demonstrated superior strength.

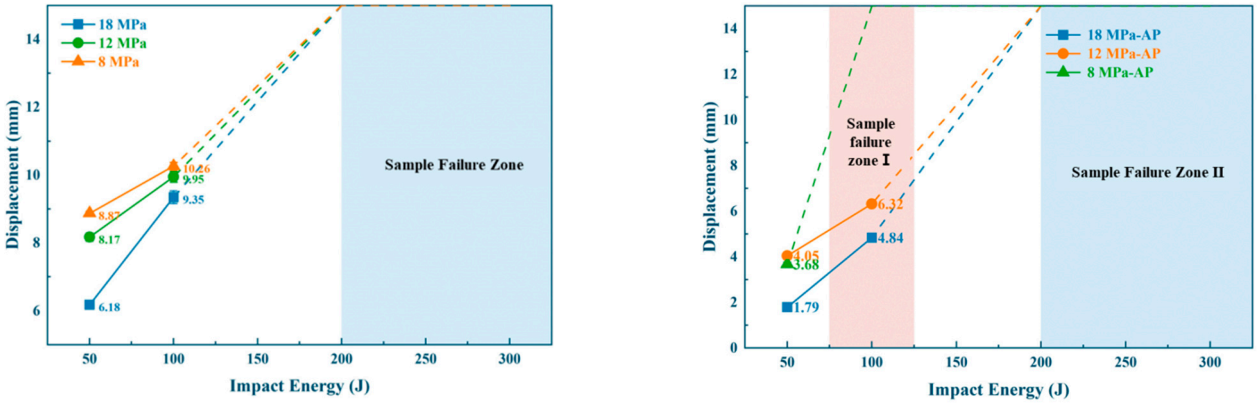

Figure 5. Impact resistance performance of aluminum honeycomb with varying static compressive strengths: (**a**) indentation deformation (mm) of aluminum honeycomb with different static compressive strengths under various impact energies; (**b**) indentation deformation (mm) of the aluminum plate in contact with aluminum honeycomb with varying static compressive strengths under different impact energies. The dashed line indicates that the aluminum honeycomb is completely broken down and fails when the specific impact energy is higher than this.

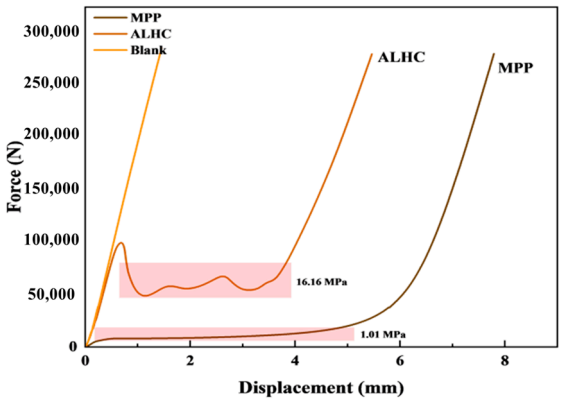

Figure 6. Force–displacement curves of different core materials under impact.

Table 4. Static compressive strength and compression ratio of different core materials.

Material	Static Compressive Strength	Compression Ratio
Aluminum honeycomb	16.16 MPa	89.58%
MPP	1.01 MPa	77.82%

Steel plates are the primary energy-absorbing components in multi-material protective plate structures, providing overall support and reinforcement. Upon impact, the steel plate initially deforms elastically. As the impact force increases, the plate undergoes plastic deformation, which is the main energy absorption mechanism. Therefore, the higher the yield strength of the steel plate, the less deformation occurs under impact. As illustrated in Figure 7a, with an increase in both tensile strength and impact energy, the indentation deformation of the steel plate decreased as the tensile strength rose. Similarly, Figure 7b shows a comparable trend for the indentation deformation of the aluminum plate in contact

with the steel plate. For every 25% increase in tensile strength, the impact resistance of the steel plate improved by an average of 4% to 5%, based on the indentation of the aluminum plate at a 300 J impact.

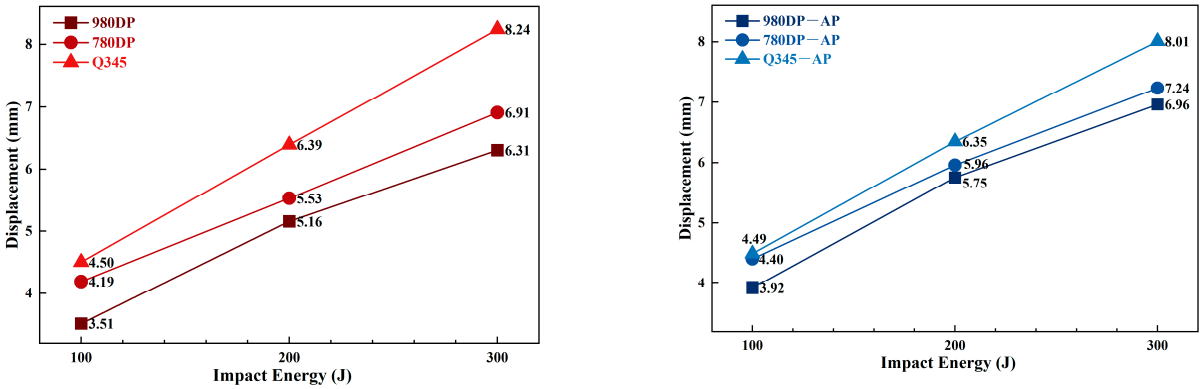

(**a**) (**b**)

Figure 7. Impact resistance of steel plates with varying tensile strengths: (**a**) indentation deformation (mm) of steel plates with different tensile strengths under various impact energies; (**b**) indentation deformation (mm) of the aluminum plate in contact with steel plates of varying tensile strengths under different impact energies.

After conducting a series of impact resistance tests on a single material in the protective plate mentioned above, we calculated the critical values of actual fracture failure for each material when facing different impact energies. Combined with simulation data, we obtained the actual energy absorption ratio of each material under 400J impact energy, as shown in Figure 8. In the preliminary experiments, the impact resistance performance of the steel plate single material was excellent in the drop hammer impact test, with a comprehensive energy absorption ratio of up to 34.3%, followed by the energy absorption ratio of the simulated battery cell substitute (aluminum honeycomb), which also reached 29.1%.

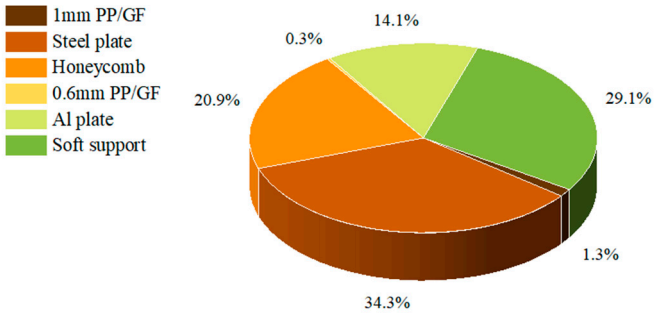

Figure 8. Energy absorption proportions of different materials in the protective plate during impact.

2.2. Protective Plate Drop-Weight Impact Test

The relationship between the tensile strength of the steel plate and the overall impact resistance of the protective plate is presented in Table 5 and Figure 9. It is observed that a 25.64% increase in the steel plate strength within the protective plate resulted in a reduction in damage depth of approximately 2.40% at an impact energy of 400 J and 5.07% at 300 J. However, the improvement in overall impact resistance due to the increased steel plate strength is somewhat diminished. In protective plates containing 980DP steel, the resulting indentation on the aluminum plate remained approximately 4 mm.

Table 5. Influence of steel plate strength on the impact resistance of the protective plate.

Type of Steel Plate	Impact Depression Degree of Aluminum Plate (Impact Energy 300 J)	Impact Depression Degree of Aluminum Plate (Impact Energy 400 J)
980DP	3.35 mm	4.17 mm
780DP	3.18 mm	4.07 mm

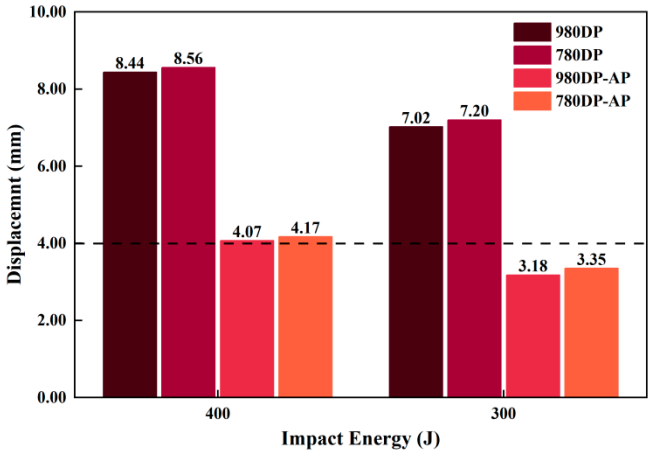

Figure 9. Impact resistance of protective plates with different steel types.

Figure 10 shows the deformation of the protective plate surface and the aluminum plate and soft support in direct contact with it at different impact energy levels. It can be clearly observed that the depth and range of the pits formed by the 300 J impact are less than those of the 400 J impact. In the test, each impact was at least 100 mm apart, which ensures the accuracy of each test's data and is not affected by the previous impact.

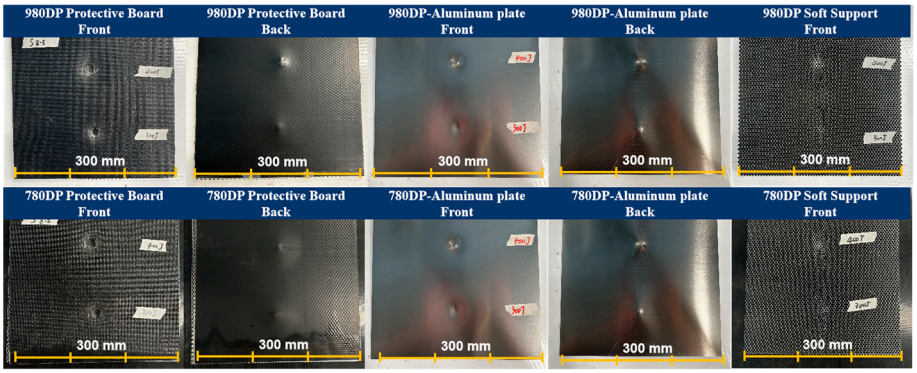

Figure 10. Photographs of protective plate samples post-impact testing for various steel types.

From Figure 11a, it can be observed that when the tensile strength of the steel plate in the protective layer was 980 MPa, the compressive strength of the aluminum honeycomb core significantly influenced the impact resistance, particularly when the impact energy exceeded 300 J. At an impact energy of 400 J, a reduction in the static compressive strength of the honeycomb core from 18 MPa to 12 MPa resulted in an increase in the indentation of the protective plate (comparing the 18 MPa and 12 MPa curves) by approximately 8.89% to 11.9% and a corresponding increase in the indentation of the aluminum plate (18 MPa-AP vs. 12 MPa-AP) by about 22.3% to 27.3%. This observation is consistent with previous experiments on steel plate specimens. In Figure 11b, for a steel plate with a tensile strength of 780 MPa paired with aluminum honeycomb cores of varying static compressive strengths, the overall impact resistance of the protective plate shows minimal

variation (differences ranging from 0.93% to 22.0%). Under a 300 J impact, the high-strength aluminum honeycomb cores nearly collapsed; therefore, at 400 J, the differences in the steel plate strength primarily governed the deformation behavior in the later stages of impact.

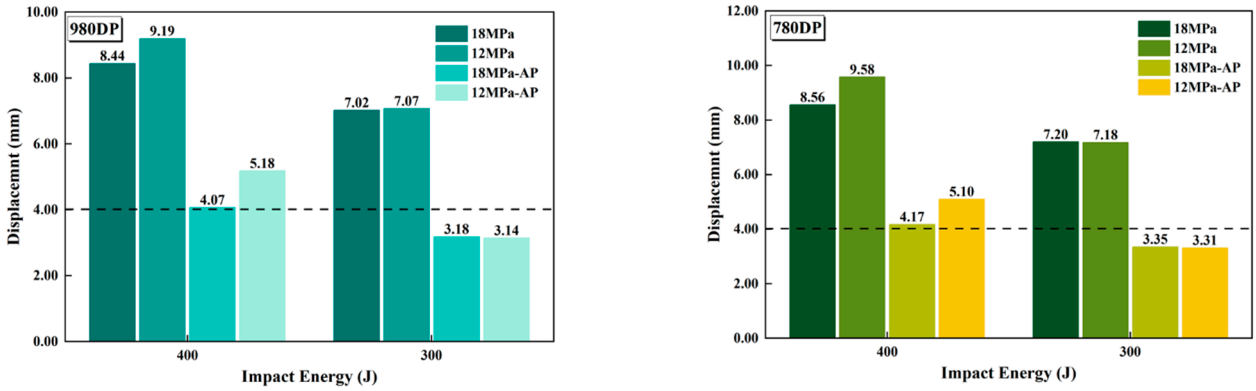

(**a**) (**b**)

Figure 11. Impact resistance of protective plates with varying aluminum honeycomb compressive strengths: (**a**) indentation deformation (mm) of protective plates with honeycomb cores of different static compressive strengths under various impact energies; (**b**) indentation deformation (mm) of the aluminum plate in contact with protective plates containing honeycomb cores with varying static compressive strengths under different impact energies.

In order to investigate the effect of honeycomb core thickness on the overall impact resistance of the protective plate in the sandwich structure of the protective plate, as shown in Table 6, we prepared five sets of protective plate samples with different honeycomb core thicknesses. The thickness difference between the three groups is 2mm, and the thickness difference between the last two groups is 3mm. This can more significantly obtain the influence of honeycomb core thickness, weight, and total thickness of the protective plate on the protective effect. As shown in Figure 12a, the deformation of the protective plate under impact increased progressively with the thickness of the honeycomb core. Notably, in Figure 12b, when the honeycomb core thickness reaches 12 mm or more, the deformation of the corresponding aluminum plate (12 MPa–12 mm AP curve) under a 400 J impact becomes almost negligible (around 1.0 mm). However, as the honeycomb core thickness continued to increase, the overall deformation of the protective plate increased significantly. This is due to the energy absorption through compressive deformation of the honeycomb, and for each 1.0 mm increase in core thickness, the weight of the protective plate increased by approximately 20 g. Therefore, a balance must be maintained between the need for lightweight design and adequate impact resistance.

Table 6. Comparison of mass for honeycomb cores with varying thicknesses.

Honeycomb Core Thickness (mm)	Honeycomb Core Dimensions (mm)	Honeycomb Core Mass (kg)
5	300 × 300	0.12
7		0.16
9		0.20
12		0.25
15		0.30

The sandwich structure of the protective plate relies on adhesive films to bond the layers, creating an integrated unit that enhances the overall strength and stiffness of the composite. Figure 13 shows the deformation and damage morphology of each layer structure of the non-adhesive protective board after being impacted. As illustrated in

Figure 14, when no adhesive bonding was applied, a 400 J impact caused significant cracks to form on the surface of the steel plate, the honeycomb core (ALHC) was crushed, and the indentation reached 10.96 mm. In contrast, the indentation of the aluminum plate increased by 74.5% compared to the specimen with adhesive bonding. Therefore, the adhesive plays a crucial role in enabling the layers to function synergistically for energy absorption.

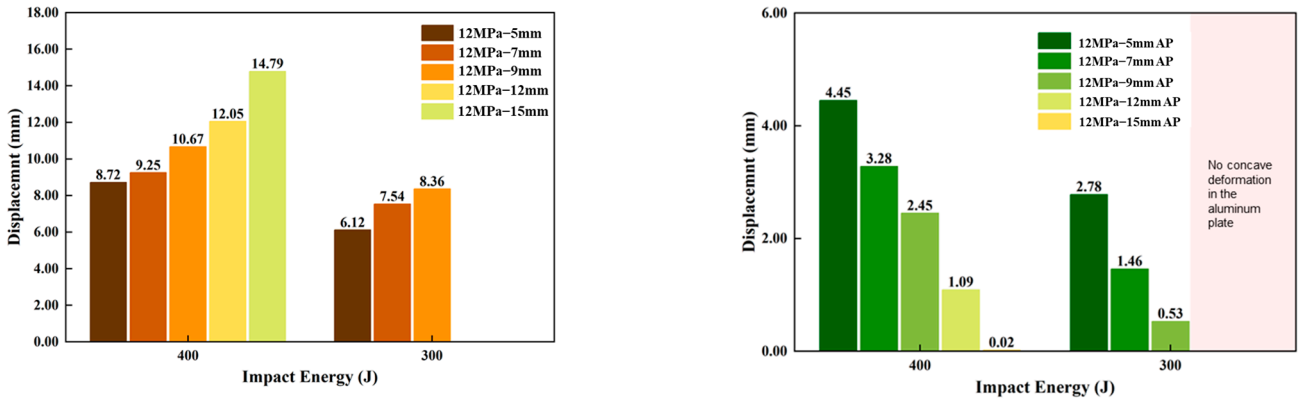

(**a**) (**b**)

Figure 12. Impact resistance of protective plates with different honeycomb core thicknesses: (**a**) indentation deformation (mm) of protective plates with honeycomb cores of varying thicknesses under different impact energies; (**b**) indentation deformation (mm) of the aluminum plate in contact with protective plates containing honeycomb cores with varying thicknesses under different impact energies.

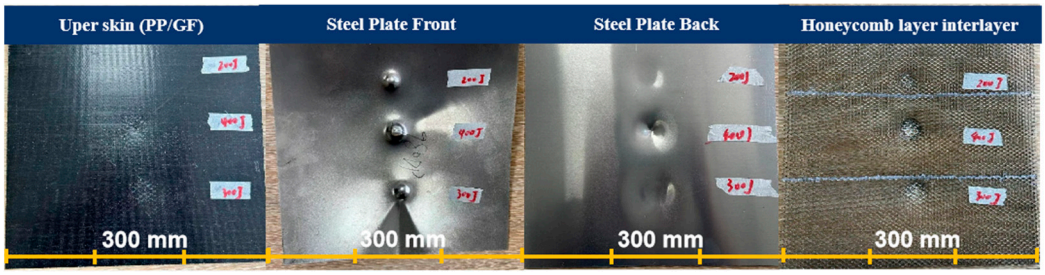

Figure 13. Post-test images of layers in a protective plate sample without adhesive bonding.

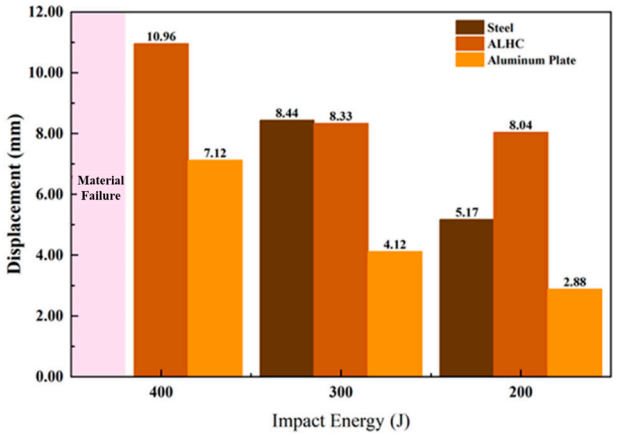

Figure 14. Impact resistance performance of a protective plate without adhesive bonding.

3. Static Pressure Trace Test

The impact generated by the hammerhead results in the formation of penetration waves, as well as lateral shear and bending waves. Based on the duration of the impact, the

responses can be categorized into ballistic, high-speed, and low-speed impacts. In the case of low-speed impacts, the duration significantly exceeds the transition times of all the stress waves, allowing the response to be analyzed in a quasi-static manner. Several studies [34,35] have shown experimentally that quasi-static indentation tests provide insights into the initiation and development of damage in composites under compression [36], thereby facilitating a better understanding of damage propagation. Moreover, these tests also capture the nonlinear mechanical behavior of composites under such loading conditions, such as the nonlinearity observed in stress–strain curves, which allows for more precise predictions of dynamic impact responses. Consequently, the quasi-static indentation method can be utilized as a reference for predicting and assessing damage in dynamic impact scenarios. Furthermore, due to the easier control of loading rates and magnitudes in quasi-static tests compared to dynamic impact tests, it is possible to apply the desired load with greater accuracy. Since the damage and responses observed in quasi-static compression tests are analogous to those from low-speed impact tests, the state of the protective plate under quasi-static indentation can be extrapolated to dynamic impact conditions.

Quasi-static compression tests were conducted on the protective plate using a universal testing machine. The specimen was secured between rigid upper and lower fixtures made from # 45 steel, which were bolted together and supported on the test platform. A hemispherical hammerhead, with a diameter of 25 mm, was used for the test, and the loading rate was set to 20 mm/min. The test was stopped once a predetermined displacement (i.e., the intrusion depth of the hammerhead) was reached. Consistent with the drop-weight impact test setup, the protective plate was placed on a 1.5 mm thick aluminum plate, with a soft honeycomb core beneath it, with a compressive strength of 12 MPa. During each test, the corresponding indentation of the aluminum plate at the specified displacement was recorded.

As illustrated in Figure 15a, after the steel plate fractured and the force–displacement curve showed a sharp peak, continued intrusion caused the hammerhead to compress the honeycomb core beneath the steel plate, resulting in a brief stress plateau. As the intrusion progressed further, the honeycomb core was completely crushed, and the force continued to rise until the preset displacement was achieved. For the 0.8 mm thick 980DP steel plate, fracture occurred when the hammerhead intrusion reached approximately 7.85 mm, while for the 0.8 mm thick 1180DP steel plate, fracture occurred at around 9.02 mm, as shown in Figure 15b. By integrating the force–displacement curves from the quasi-static tests, it was determined that the 0.8 mm 980DP steel plate absorbed an average energy of 130.5 J at the point of fracture, while the 0.8 mm 1180DP steel plate absorbed about 153.8 J before fracture, showing a 17.5% difference in energy absorption, which correlates with the disparity in tensile strength between the two steels.

Figure 16a–c demonstrate that after compression, the energy absorption of the steel plate in the protective plate meets the expected results. As the steel plate thickness increased, the overall energy absorption threshold of the protective plate increased significantly. The steel plate plays a crucial role in enhancing the energy absorption of the multi-material protective plate, and the energy absorbed by the steel plate before fracture is taken as a representative measure of the total energy absorption. As shown in the curve in Figure 16a,b, the two main factors influencing the energy absorption of the protective plate are the maximum deformation of the steel plate at fracture and the maximum applied load. When the steel plate thickness is increased—particularly above 1.5 mm—the hammer head intrusion exceeds 10.3−10.4 mm. As depicted in Figure 16c, when the steel plate thickness reaches 2.0 mm, the hammer head must intrude 12.3 mm to penetrate the steel plate. At this point, the combined energy absorption of the protective plate and the underlying soft support reaches nearly 520 J.

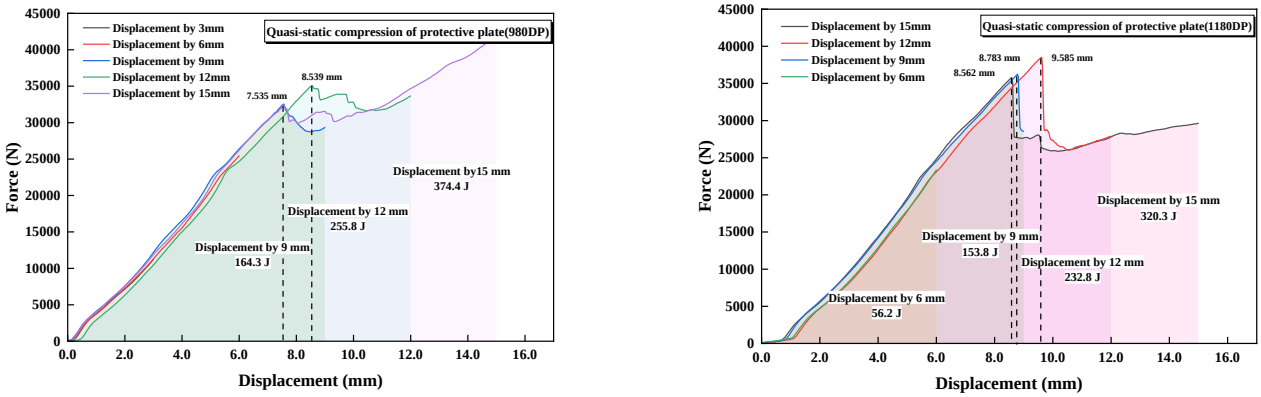

Figure 15. Force–displacement curves under quasi-static compression for protective plates with varying steel strengths: (**a**) force–displacement curves and energy absorption at different stages for a protective plate with 980DP steel under quasi-static compression; (**b**) force–displacement curves and energy absorption at different stages for a protective plate with 1180DP steel under quasi-static compression.

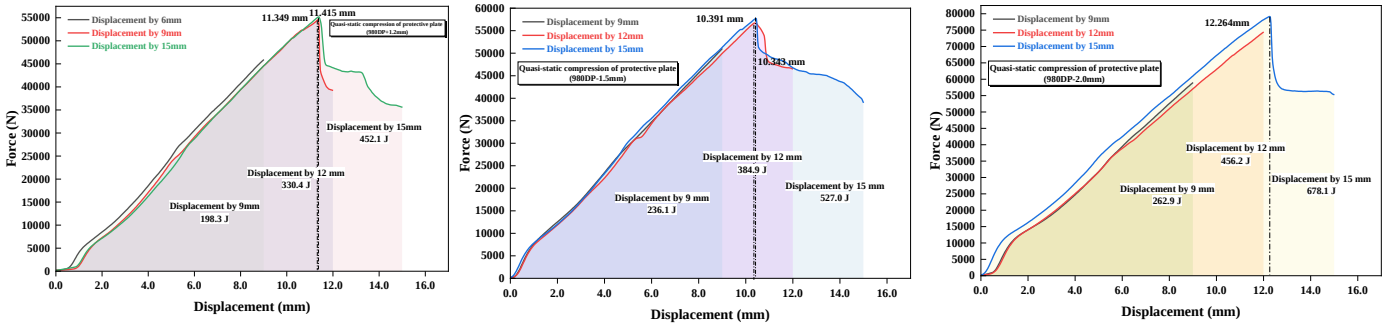

Figure 16. Force–displacement curves under quasi-static compression for protective plates with varying steel plate thicknesses: (**a**) force–displacement curves and energy absorption for a protective plate with 1.2 mm thick 980DP steel under quasi-static compression; (**b**) force–displacement curves and energy absorption for a protective plate with 1.5 mm thick 980DP steel under quasi-static compression; (**c**) force–displacement curves and energy absorption for a protective plate with 2.0 mm thick 980DP steel under quasi-static compression.

4. Analysis of Equivalence Between Drop-Weight Impact and Quasi-Static Compression

Static process analysis describes the long-term response of a structure subjected to a specific load, accurately representing the behavior when acceleration is negligible. In dynamic impact processes, the influence of acceleration is substantial and cannot be overlooked, as the kinetic energy generated by acceleration is considerable. Quasi-static conditions are derived from the reduction in dynamic conditions, considering that true static conditions do not exist.

As shown in Figure 17, under impact energies ranging from 50 J to 200 J, the indentation deformation of the steel plate and the corresponding equivalent impact force began to exhibit initial cracking at an impact energy of approximately 150 J for the 980DP steel plate. In the quasi-static compression test, the hammer head displacement was 8.24 mm. Specifically, when the steel plate absorbed 120 J, fine cracks appeared at the edge of the indentation. In contrast, the high-ductile 980TBF steel plates only began to exhibit small cracks when the impact energy reached 200 J. Based on these observations, it can be preliminarily concluded that quasi-static compression induces fracture in the steel plate

more readily than dynamic impact. The equivalence ratio between quasi-static compression energy and dynamic impact energy ranges from approximately 1.2 to 1.3.

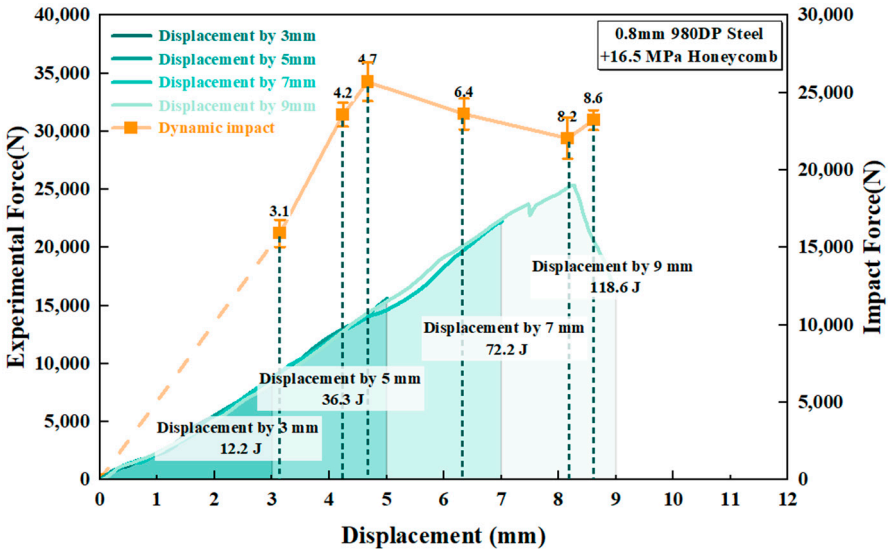

Figure 17. Comparison of energy absorption between drop-weight impact and quasi-static indentation for 980DP steel plates.

Figure 18 illustrates that when the protective plate undergoes the same level of deformation, both the drop-weight impact and quasi-static indentation curves exhibit a similar abrupt drop in force. This decrease is primarily attributed to the fracture failure of the steel plate within the protective plate. The force–displacement curve shows a sudden reduction in force at a hammer head displacement of approximately 8.10 mm, at which point the quasi-static energy absorption is about 207 J (using the quasi-static 11 mm curve as an example).

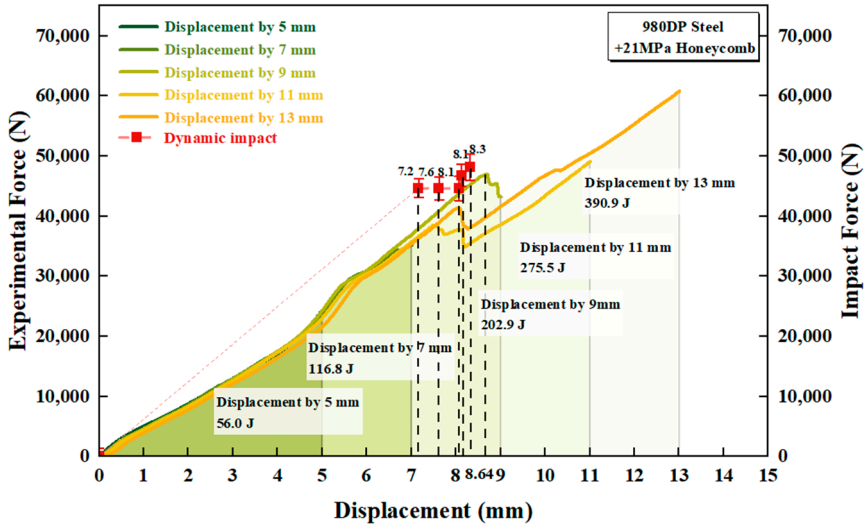

Figure 18. Comparison of energy absorption between drop-weight impact and quasi-static indentation for 980DP steel protective plates.

As shown in Figure 19, in the dynamic impact tests of the 980TBF steel protective plates, the calculated equivalent impact force decreased when the impact energy reached 320 J. For the quasi-static compression curve of the 980TBF protective plate, a sudden drop in force occurred when the hammer head displacement was between 9.00 and 9.88 mm, with the quasi-static energy absorption being approximately 275 J (using the quasi-static 11 mm

curve as a reference). Similarly, the dynamic impact curve also exhibited a decrease in the equivalent impact force at 320 J. The difference in energy absorption between dynamic impact and quasi-static compression is related to the ductility of the steel plate. For 980DP steel, this difference was approximately 100 J, whereas for 980TBF steel, the difference was only about 50 J.

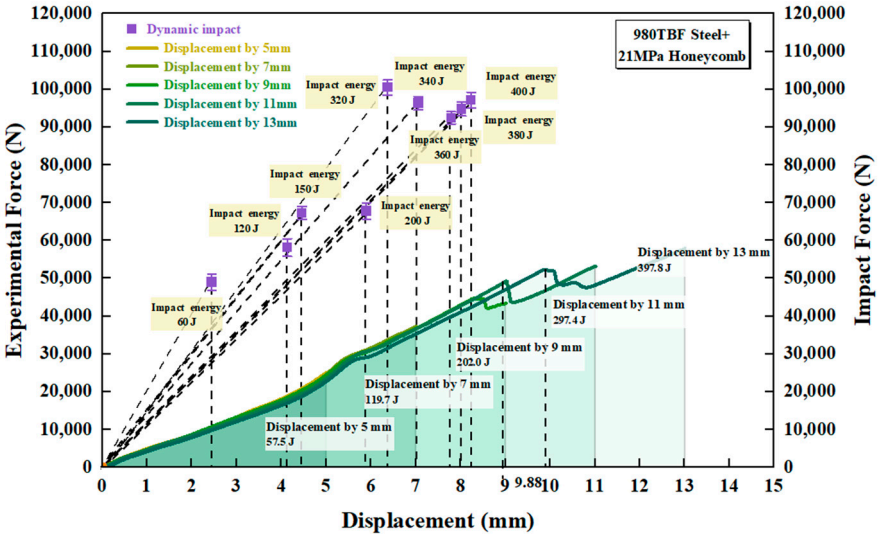

Figure 19. Comparison of energy absorption between drop-weight impact and quasi-static indentation for 980TBF steel protective plates.

5. Conclusions

An equivalent modeling approach was employed in this study to perform matrix-style drop-weight impact tests on individual material layers, as well as the complete sandwich-structured protective plate. Alongside quasi-static indentation tests, the following conclusions were drawn:

- Under the condition of a 400 J high-energy impact, the material combination of a 980DP steel plate and 21 MPa aluminum honeycomb protective plate had a self-concave deformation of only 8.44mm, and the corresponding concave deformation of the water-cooled plate was only 4.07 mm. Compared with PP honeycomb protective plate under the same conditions, its impact resistance performance was more than 50% better.
- In the case where simulated cells also participate in energy absorption, the steel plate in the protective plate that bears the main energy absorption role can account for 34.3% of the energy absorption. When only considering the energy absorption of the protective plate, the high-strength steel plate bears more than 60% of the main energy absorption effect for the impact layer, while the aluminum honeycomb energy absorption accounts for about 28%. There is a mutual reinforcement effect between the honeycomb and the steel plate, and the aluminum honeycomb increases the strain at the impact point of the steel plate, thus improving the overall energy absorption of the steel plate. Steel plates also make the edges of the honeycomb more evenly stressed, thereby increasing the compression strength of the honeycomb and enhancing its energy absorption capacity.
- The drop-hammer impact test results of the protective plate show that the tensile strength of the steel plate and the static pressure strength of the honeycomb jointly affected the depth of damage to the protective plate after impact, and the two reinforced each other. Specifically, for every 25.6% increase in steel plate strength, the average depth of damage to the protective plate decreased by 3.5%.

- The drop-hammer impact test and static pressure mark test of the protective plate have a certain equivalence. Under the same testing conditions, the resistance of the protective plate to impact damage was better than that of static pressure marks. From the perspective of energy absorption, the energy absorption of the drop-hammer impact test was about 1.2 to 1.3 times higher than that of the static indentation test.

This study focuses on the synergistic effect of multiple materials and the damage mechanism of protective plates under impact loads. In the research work, detailed performance data of various material combinations were analyzed, and after summarizing the relevant data, a protective plate structure model with the best protective effect and lightweight benefits was analyzed. There are certain limitations in the theoretical model, and future research will combine theories such as stress wave propagation and strain rate effects to analyze the dynamic response of materials in depth. In addition to mechanical performance research, the protective plate specimens also included other types of tests, such as immersion tests, salt spray corrosion resistance tests, and high- and low-temperature impact tests, which verify the high reliability of the protective plate in extreme environments. Subsequent research will focus on exploring the long-term performance of materials in different environments, especially weather resistance and aging resistance, to ensure their stability and reliability throughout their entire lifecycle. The performance changes of materials in complex environments will be analyzed to provide more comprehensive theoretical support and data reference for the design of protective panels for new energy vehicle battery packs.

Author Contributions: In the process of writing the paper, all the authors made important contributions. C.L. was responsible for the overall design of the study and the formulation of the experimental scheme and participated in part of the experimental operation and data analysis. J.Z. was mainly responsible for the collection and collation of experimental data and made a preliminary analysis of the experimental results. R.S. focused on the writing and revision of the paper and conducted in-depth elaboration and discussion on the research content. Other authors also provided professional advice and guidance in their respective research fields and made positive contributions to the improvement of the paper. All authors have read and agreed to the published version of the manuscript.

Funding: This research was supported by the Shenzhen Science and Technology Program (Project No. KJZD20230923114259049), for which we express our heartfelt thanks.

Data Availability Statement: The original contributions presented in this study are included in the article. Further inquiries can be directed to the corresponding author.

Acknowledgments: This research was supported by the Shenzhen Science and Technology Program (Project No. KJZD20230923114259049), for which we express our heartfelt thanks. The support of the fund provided important help for the research and made project completion successful.

Conflicts of Interest: Author C.L. was employed by the company Shenzhen CANSINGA Technology. The remaining authors declare that the research was conducted in the absence of any commercial or financial relationships that could be construed as a potential conflict of interest.

References

1. Yuan, X.; Liu, X.; Zuo, J. The development of new energy vehicles for a sustainable future: A review. *Renew. Sustain. Energy Rev.* **2015**, *42*, 298–305. [CrossRef]
2. Muratori, M.; Alexander, M.; Arent, D.; Bazilian, M.; Cazzola, P.; Dede, E.M.; Farrell, J.; Gearhart, C.; Greene, D.; Jenn, A.; et al. The rise of electric vehicles—2020 status and future expectations. *Prog. Energy* **2021**, *3*, 022002. [CrossRef]
3. Kumar, A. A comprehensive review of an electric vehicle based on the existing technologies and challenges. *Energy Storage* **2024**, *6*, e70000. [CrossRef]
4. Ralls, A.M.; Leong, K.; Clayton, J.; Fuelling, P.; Mercer, C.; Navarro, V.; Menezes, P.L. The role of lithium-ion batteries in the growing trend of electric vehicles. *Materials* **2023**, *16*, 6063. [CrossRef] [PubMed]

5. Belingardi, G.; Scattina, A. Battery pack and underbody: Integration in the structure design for battery electric vehicles—Challenges and solutions. *Vehicles* **2023**, *5*, 498–514. [CrossRef]
6. Arora, S.; Shen, W.; Kapoor, A. Review of mechanical design and strategic placement technique of a robust battery pack for electric vehicles. *Renew. Sustain. Energy Rev.* **2016**, *60*, 1319–1331. [CrossRef]
7. Xia, Y.; Wierzbicki, T.; Sahraei, E.; Zhang, X. Damage of cells and battery packs due to ground impact. *J. Power Sources* **2014**, *267*, 78–97. [CrossRef]
8. Sun, P.; Bisschop, R.; Niu, H.; Huang, X. A review of battery fires in electric vehicles. *Fire Technol.* **2020**, *56*, 1361–1410. [CrossRef]
9. Chavan, S.; Venkateswarlu, B.; Prabakaran, R.; Salman, M.; Joo, S.W.; Choi, G.S.; Kim, S.C. Thermal runaway and mitigation strategies for electric vehicle lithium-ion batteries using battery cooling approach: A review of the current status and challenges. *J. Energy Storage* **2023**, *72*, 108569. [CrossRef]
10. Xie, L.; Ustolin, F.; Lundteigen, M.A.; Li, T.; Liu, Y. Performance analysis of safety barriers against cascading failures in a battery pack. *Reliab. Eng. Syst. Saf.* **2022**, *228*, 108804. [CrossRef]
11. Vimmerstedt, L.J.; Ring, S.; Hammel, C.J. *Current Status of Environmental, Health, and Safety Issues of Lithium Ion Electric Vehicle Batteries*; NREL/TP-463-7673; USDOE: Washington, DC, USA, 1995.
12. Zhou, Z.; Liu, Y.; Liao, W.; Yang, G.; Jiang, H.; Sang, J.; Tian, W.; Chai, L. Investigation on the Effect of Energy Release Rate of Aluminized Explosive on the Damage of Underwater Targets. *Propellants Explos. Pyrotech.* **2024**, *49*, e202300312. [CrossRef]
13. Gong, C.; Liu, J.; Han, Y.; Hu, Y.; Yu, H.; Zeng, R. Safety of electric vehicles in crash conditions: A review of hazards to occupants, regulatory activities, and technical support. *IEEE Trans. Transp. Electrif.* **2021**, *8*, 3870–3883. [CrossRef]
14. Duan, J.; Tang, X.; Dai, H.; Yang, Y.; Wu, W.; Wei, X.; Huang, Y. Building safe lithium-ion batteries for electric vehicles: A review. *Electrochem. Energy Rev.* **2020**, *3*, 1–42. [CrossRef]
15. Ould Ely, T.; Kamzabek, D.; Chakraborty, D. Batteries safety: Recent progress and current challenges. *Front. Energy Res.* **2019**, *7*, 71. [CrossRef]
16. Khan, M.; Yan, S.; Ali, M.; Mahmood, F.; Zheng, Y.; Li, G.; Liu, J.; Song, X.; Wang, Y. Innovative solutions for high-performance silicon anodes in lithium-ion batteries: Overcoming challenges and real-world applications. *Nano-Micro Lett.* **2024**, *16*, 179. [CrossRef]
17. Wei, L.; Gao, Z. Recent research advances on corrosion mechanism and protection, and novel coating materials of magnesium alloys: A review. *RSC Adv.* **2023**, *13*, 8427–8463. [CrossRef]
18. Liu, Y.; Pan, Y.; Wang, H.; Li, H.; Bao, H.; Zhao, Z.; Liu, B. Mechanical issues of lithium-ion batteries in road traffic conditions: A review. *Thin-Walled Struct.* **2024**, *201*, 111985. [CrossRef]
19. Gomes, V.B.; Kasaei, M.M.; Carbas, R.J.; Marques, E.A.; da Silva, L.F. A new joining by forming process for busbar-prismatic cell interconnections in electric vehicle batteries. *Int. J. Adv. Manuf. Technol.* **2025**, *137*, 2405–2432. [CrossRef]
20. Czerwinski, F. Current trends in automotive lightweighting strategies and materials. *Materials* **2021**, *14*, 6631. [CrossRef]
21. Dou, L.; He, L.; Yin, Y. Numerical investigation on protective mechanism of metal cover plate for alumina armor against impact of fragment by FE-converting-SPH method. *Materials* **2023**, *16*, 3405. [CrossRef]
22. Li, D. Lightweight Concept Design of Economical FRTP-Metal Multi-Material Vehicle Doors. Ph.D. Thesis, Universität Siegen, Siegen, Germany, 2021.
23. Paramasivam, C.; Venugopal, R. Design and development of glass/basalt fiber reinforced composite material for automobile applications. *J. Ind. Text.* **2022**, *51* (Suppl. S1), 1668S–1681S. [CrossRef]
24. Cahyono, S.I.; Widodo, A.; Anwar, M.; Diharjo, K.; Triyono, T.; Hapid, A.; Kaleg, S. Light-weight sandwich panel honeycomb core with hybrid carbon-glass fiber composite skin for electric vehicle application. *AIP Conf. Proc.* **2016**, *1717*, 040025.
25. Yang, Y.; Miao, Z.; Liu, Y.; Tu, H.; Wei, Y. A comprehensive review of fiber-reinforced polymer-matrix composites under low-velocity impact. *Mech. Adv. Mater. Struct.* **2025**, 1–39. [CrossRef]
26. Isaac, C.W.; Ezekwem, C. A review of the crashworthiness performance of energy absorbing composite structure within the context of materials, manufacturing and maintenance for sustainability. *Compos. Struct.* **2021**, *257*, 113081. [CrossRef]
27. Peng, A.; Deng, J.; Wu, D.; Zhang, N.; Guo, Y.; Cai, D.; Zhou, G.; Wang, X. Damage behavior and failure mechanism of composite sandwich panel subjected to localized impact: A comprehensive study. *Thin-Walled Struct.* **2023**, *192*, 111155. [CrossRef]
28. Liu, C.; Teng, X.; Shi, D.; Lv, S.; Duan, Y.; Sun, Y.; Yang, X. Failure analysis and engineering mechanics modeling methods of a stitched ceramic sandwich structure. *Eng. Fail. Anal.* **2023**, *149*, 107275. [CrossRef]
29. Han, X.; Cai, H.; Sun, J.; Wei, Z.; Huang, Y.; Wang, A. Numerical studies on failure mechanisms of all-composite sandwich structure with honeycomb core under compression and impact loading conditions. *Polymers* **2022**, *14*, 4047. [CrossRef] [PubMed]
30. Shi, Y.; Pinna, C.; Soutis, C. Modelling impact damage in composite laminates: A simulation of intra-and inter-laminar cracking. *Compos. Struct.* **2014**, *114*, 10–19. [CrossRef]
31. *ASTM D7136/D7136M-23*; ASTM International. Standard Test Method for Measuring the Damage Resistance of a Fiber-Reinforced Polymer Matrix Composite to a Drop-Weight Impact Event. ASTM International: West Conshohocken, PA, USA, 2023.

32. Wu, S.; Chen, Y.; Luan, W.; Chen, H.; Huo, L.; Wang, M.; Tu, S.T. A Review of Multiscale Mechanical Failures in Lithium-Ion Batteries: Implications for Performance, Lifetime and Safety. *Electrochem. Energy Rev.* **2024**, *7*, 35. [CrossRef]
33. Mohammadi, H.; Ahmad, Z.; Mazlan, S.A.; Faizal Johari, M.A.; Siebert, G.; Petrů, M.; Rahimian Koloor, S.S. Lightweight glass fiber-reinforced polymer composite for automotive bumper applications: A review. *Polymers* **2022**, *15*, 193. [CrossRef]
34. Lei, Z.X.; Ma, J.; Sun, W.K.; Yin, B.B.; Liew, K.M. Low-velocity impact and compression-after-impact behaviors of twill woven carbon fiber/glass fiber hybrid composite laminates with flame retardant epoxy resin. *Compos. Struct.* **2023**, *321*, 117253. [CrossRef]
35. Li, J.; Zhang, W.; Wang, Z.; Wang, Q.; Wu, T.; Qin, Q. Dynamic response and failure of CFRP Kagome lattice core sandwich panels subjected to low-velocity impact. *Int. J. Impact Eng.* **2023**, *181*, 104737. [CrossRef]
36. Tabiei, A.; Zhang, W. Composite laminate delamination simulation and experiment: A review of recent development. *Appl. Mech. Rev.* **2018**, *70*, 030801. [CrossRef]

Disclaimer/Publisher's Note: The statements, opinions and data contained in all publications are solely those of the individual author(s) and contributor(s) and not of MDPI and/or the editor(s). MDPI and/or the editor(s) disclaim responsibility for any injury to people or property resulting from any ideas, methods, instructions or products referred to in the content.